J. Mech. Phys. Solids 193 (2024) 105854

Contents lists available at ScienceDirect

Journal of the Mechanics and Physics of Solids

journal homepage: www.elsevier.com/locate/jmps

Nonlinear dynamics of a flexible rod partially sliding in a rigid sleeve under the action of gravity and configurational force

Yury Vetyukov [a,*,1], Alexander Humer [b,1], Alois Steindl [a,1]

[a] Institute of Mechanics and Mechatronics, Technische Universitat Wien, Getreidemarkt 9, Vienna, 1060, Austria
[b] Institute of Technical Mechanics, Johannes Kepler University Linz, Altenberger Straße 69, Linz, 4040, Austria

ARTICLE INFO

Keywords:
Elastic rod
Moving boundary
Configurational force
Mixed Eulerian–Lagrangian description
Hamiltonian mechanics
Adiabatic invariants

ABSTRACT

We investigate various methods of analyzing systems with moving boundaries, using as an example a flexible rod sliding in an ideal frictionless sleeve in the field of gravity. Special attention is paid to the configurational force acting on the rod at the sleeve opening and thus determining the rod's dynamics. The non-material kinematic description used in simulations is based on the re-parametrization of the Lagrangian arc length coordinate. The variational formulation uses the energy expressions written for the entire rod, comprising the free segment and the one inside the sleeve. A novel finite element scheme is efficient for highly flexible rods, which may undergo complete ejection. A simplified two degrees of freedom model, which accelerates simulations, shows a good agreement as the bending stiffness increases. An analytical study using Hamiltonian mechanics exploits the separation of variables into fast oscillations and slow axial motion. The adiabatic invariant approach leads to approximate closed-form solutions for the slow dynamics and yields the maximum injection depth of the rod into the sleeve.

1. Introduction

A growing body of literature is devoted to the mechanics of flexible rods, partially sliding in a rigid sleeve. The conventional idealization implies the rod particles to be moving only along the axial direction when inside the sleeve, while kinematic constraints are released as soon as the particle leaves the sleeve and transitions into a free segment. This continued exchange of particles between the two qualitatively different domains, i.e., the free segment and the one within the sleeve, results into various non-trivial mechanical phenomena, both in dynamics and in quasi-statics. Such processes feature moving discontinuities, thus requiring a thorough treatment of basic principles of mechanics as well as novel numerical and analytical methods for mathematical modeling.

It is often reasonable to assume the axial motion of the rod within the sleeve to be kinematically imposed, such that the particles enter or leave the free segment with a given time rate. This will be the case, e.g., in reeving or hoisting systems, when a cable is released from a roller with constant angular velocity (Escalona et al., 2018; Kaczmarczyk and Ostachowicz, 2003). The classic "sliding spaghetti" problem, when the vibrations of a beam increase as it is getting "sucked" into a sleeve, was investigated by Vu-Quoc and Li (1995), Humer et al. (2020), Boyer et al. (2022), the reverse "spaghetti problem" by Mansfield and Simmonds (1987); see also (Steinbrecher et al., 2017) for a validation against a more computationally expensive solution of a contact problem with a finite gap between the rod and the walls of the sleeve. As shown in Vetyukov (2021), the frictional contact may cause a non-trivial transient dynamics of such an axially transported beam even when inertia is neglected, i.e. in the quasi-statics; see also a review on mechanics of axially moving structures, Scheidl and Vetyukov (2023).

* Corresponding author.
E-mail addresses: yury.vetyukov@tuwien.ac.at (Y. Vetyukov), alexander.humer@jku.at (A. Humer), alois.steindl@tuwien.ac.at (A. Steindl).
[1] All authors contributed equally to this work.

https://doi.org/10.1016/j.jmps.2024.105854
Received 24 May 2024; Received in revised form 21 August 2024; Accepted 5 September 2024
Available online 11 September 2024

If the axial motion in the sleeve is not prescribed kinematically but rather results from the interaction with the free segment, the sliding-rod problem becomes even more challenging. The energy release rate for a rod sliding within an ideal sleeve and with deformed free part proves the existence of a force in outward direction, which pushes the rod out of the sleeve. This force (which we call configurational) equals the energy density of bending of the rod at the opening of the sleeve (thus being proportional to the square of the bending moment), see Bigoni et al. (2022). An interpretation on the level of Newtonian mechanics requires the limiting transition in the contact problem for the more realistic setting of a small but non-vanishing gap between the rod and the sleeve (Bigoni et al., 2015). This force is, for example, responsible for the sliding of a flexible rod out of a horizontal frictionless channel as soon as the free part of the rod bends due to gravity. The terms "Eshelby-like" or "material" force are also in use and reflect the relation to the problems of crack growth and motion of dislocations in solid fracture mechanics, for which the apparatus of analytical mechanics with generalized coordinates and work done by conjugate forces was proven to be advantageous (Kienzler and Herrmann, 2000). The notion of configurational forces explains interesting phenomena in structural mechanics such as the experimentally validated functioning of an elastica arm scale (Bosi et al., 2014); we also refer to the comprehensive treatise by O'Reilly (2017), the general discussion of configurational mechanics by Steinmann (2008), as well as the relevant problem formulations and interesting analysis in Singh and Hanna (2017). A thorough investigation of the phenomenon of the configurational force from the perspective of a 2D continuum model of the rod has recently been presented by Dal Corso et al. (2024).

Among various appearances of configurational forces in structural dynamics, we focus on the dancing rod problem, introduced by Armanini, Dal Corso, Misseroni, and Bigoni (2019); see also a recent extension in Koutsogiannakis et al. (2023). A flexible rod, partially inserted into an inclined rigid sleeve with no or little friction exhibits rich motion in the presence of gravity, during which injection turns into ejection and vice versa. The dynamic process can even end up in the full ejection of the rod. The experimental observation is supported by an analytical model based on the principles of Newtonian mechanics, simplified by the assumption that the entire mass of the moving rod is concentrated at its tip, thus resulting in a model with two degrees of freedom. Recently, Han (2022), Han and Bauchau (2023) numerically addressed a similar problem for a rod with distributed mass. They formulated the equations of motion in variational form for the free and for the constrained segments separately, thus treating two open systems with additional interaction terms at the boundary between them, see also Irschik and Holl (2002) for the discussion of the flux terms in the analytical mechanics of deformable bodies. Neglecting friction, Han and Bauchau validated their computations against the dynamic simulation of the contact problem using Abaqus and obtained a very good matching.

In the first part of the present paper, we develop a particularly simple mathematical model that treats the entire dancing rod as a whole body with a moving boundary between the two segments, thus avoiding the burden of dealing with open systems. Using a solution-dependent coordinate transformation for the free segment of the rod, we parametrize its deformed shape using a non-material finite element approximation in the spirit of the mixed Eulerian–Lagrangian kinematic description (Pechstein and Gerstmayr, 2013; Humer, 2013; Humer et al., 2020; Vetyukov, 2018; Scheidl and Vetyukov, 2023). In addition to the nodal unknowns, degrees of freedom include the axial displacement of the rod inside the sleeve. We assume a flexible and thin rod to be inextensible and unshearable, which requires the approximation of the deformed centerline in the free segment to be smooth (Vetyukov, 2012). Deriving the kinetic energy, strain energy and gravity potential by adding up the contributions from the free segment and the one within the sleeve, we write down Lagrange equations of motion of the second kind, which can be integrated over time. Numerical simulations are successfully validated against Han and Bauchau (2023). Although the model does not require the expression for the configurational force to be explicit, it is taken into account by the formalism of analytical mechanics and can be evaluated at the stage of post-processing — just like the reactions of ideal constraints.

The vibration amplitude in the free segment gets smaller and the frequency grows as we increase the bending stiffness of the rod. Focusing on this case, in the second part of the paper we derive an analytical solution of the equations of motion for a simplified model with just two degrees of freedom. The first degree of freedom describes the axial motion of the rod, while the second represents the transverse vibration of its free segment. The single-term Ritz approximation of the transverse bending makes use of either the first vibration mode or the static deflection of a cantilever under distributed load as the shape function. A nonlinear system of equations of motion results from relatively simple energy expressions and can be easily integrated numerically. Assuming the axial motion of the rod to be significantly slower than the transverse oscillations, it was possible to treat the equations analytically using the theory of adiabatic invariants for Hamiltonian systems (Arnol'd, 1963). The perturbation method provides a relation for the vibration amplitude and its frequency, determined by the axial motion, allowing to derive a closed-form expression for the maximum depth of injection of the rod into the sleeve for given initial conditions. Analytical conclusions are in a good correspondence with the results of finite element simulations.

2. Mathematical model of the dancing rod

2.1. Problem statement

The mechanical system featuring plane motion of a flexible elastic rod partially sliding in a rigid sleeve is shown in Fig. 1. The axis of the sleeve x is inclined relative to gravity g by the angle α. The total length of the rod is ℓ; it is inextensible and unshearable; its bending rigidity is a and the mass per unit length is ρ. The length of the free part of the rod outside the sleeve $\eta(t)$ is a function of time. We assume an ideal contact model: that the segment of the rod within the sleeve of the length $\ell - \eta$ is always straight and undeformed. The contact is frictionless, which means that the mechanical system is conservative. The concentrated contact force at the tip of the sleeve, whose axial component is the configurational force N, is also assumed to be frictionless. In Newtonian mechanics, this can be explained by the orthogonality of the concentrated contact force to the slightly deformed centerline of the

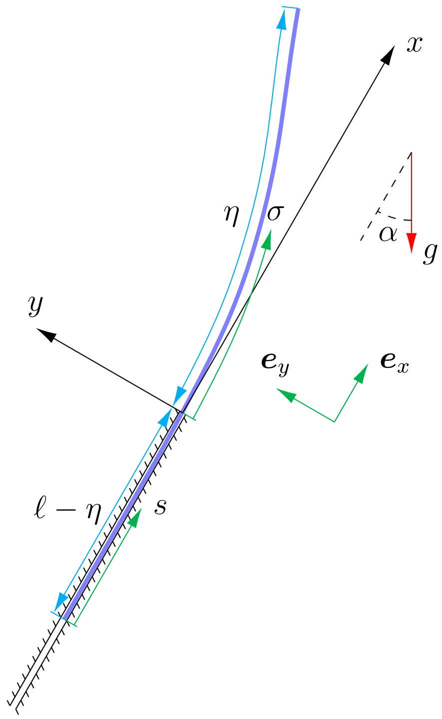

Fig. 1. Flexible rod sliding in a sleeve in the field of gravity; material coordinate s and normalized coordinate in the flexible segment σ.

rod (Bigoni et al., 2015), and thus should be classified as a reaction force of an ideal constraint, whose virtual work vanishes at all times. Although the force N is work conjugate to the length of the free segment η, the actual work is done by gravity. This is similar to the case of a mass, sliding on an inclined surface: the normal reaction of the surface performs no work, but its horizontal component is work conjugate to the horizontal motion of the mass.

2.2. Kinematic description

In the Lagrangian (material) kinematic description, the position vector of a rod's particle is a function of the material coordinate s (which is the arc length at all times and is counted from the end of the rod inside the sleeve) and time:

$$\boldsymbol{x} = x\boldsymbol{e}_x + y\boldsymbol{e}_y = \boldsymbol{x}(s,t). \tag{1}$$

This description is clearly inefficient for our actual needs because the material particles move between the constrained and free segments. An attempt to simulate the problem using conventional Lagrangian finite elements would result into numerically induced oscillations because of the necessity to apply kinematic constraints on parts of the elements, which can hardly be resolved efficiently (Steinbrecher et al., 2017; Oborin et al., 2018).

A change of variables in the spirit of mixed Eulerian–Lagrangian approach (Scheidl and Vetyukov, 2023) helps avoiding these numerical difficulties. We parametrize the deformation of the free segment of the rod by a normalized coordinate σ, which changes from 0 at the tip of the sleeve to 1 at the free (outside) end of the rod. This is somewhat similar to the notion of the mesh coordinate used by Han and Bauchau (2023). The linear mapping between this normalized non-material coordinate and the Lagrangian material coordinate is easy to establish for a given value of the length of the free segment:

$$s = \ell - \eta + \eta\sigma, \quad \sigma = 1 - \frac{\ell - s}{\eta}. \tag{2}$$

Note that

$$s|_{\sigma=0} = \ell - \eta, \quad s|_{\sigma=1} = \ell \tag{3}$$

are the current material boundaries of the free segment. The motion of the mechanical system is fully defined by the time-dependent parametrization of the free segment

$$\boldsymbol{x} = \boldsymbol{x}(\sigma,t), \quad 0 \le \sigma \le 1 \tag{4}$$

and by the time evolution of a configurational parameter $\eta(t)$. The parametrization needs to satisfy kinematic boundary conditions

$$x|_{\sigma=0} = 0, \quad y|_{\sigma=0} = 0, \quad \partial_\sigma y|_{\sigma=0} = 0, \tag{5}$$

in which we introduced a partial derivative operator

$$\partial_\sigma \equiv \frac{\partial}{\partial \sigma}. \tag{6}$$

In what follows, the inextensibility condition

$$|\partial_s \boldsymbol{x}| = 1 \tag{7}$$

is imposed using the penalty approach in the following.

2.3. Energy expressions

Obtaining the equations of motion of a conservative system using the Lagrangian formalism requires expressions of the kinetic and the potential energies. The constrained segment is undeformed, and the total strain energy of the rod is to be obtained by the integration over the free part:

$$U = \int_{\ell-\eta}^{\ell} \frac{1}{2}(a\kappa^2 + b\varepsilon^2)\,\mathrm{d}s = \int_0^1 \frac{1}{2}(a\kappa^2 + b\varepsilon^2)\eta\,\mathrm{d}\sigma. \tag{8}$$

We transformed the integral to new coordinates with the Jacobian $\partial_\sigma s = \eta$, see Eq. (2). By the transformation, we obtain an integral over a fixed domain, which is the main benefit of the non-material coordinate. The first term in parentheses is the bending energy density with the square of the curvature of the rod κ easily computed as

$$\kappa^2 = \partial_s^2 \boldsymbol{x} \cdot \partial_s^2 \boldsymbol{x} = (\partial_s^2 x)^2 + (\partial_s^2 y)^2. \tag{9}$$

Indeed, $\partial_s \boldsymbol{x}$ is a unit tangent vector because s remains the arc length coordinate according to the inextensibility condition. Therefore, the second derivative $\partial_s^2 \boldsymbol{x}$ is a unit normal multiplied by the curvature. The second term in brackets in Eq. (8) corresponds to the energy density induced by extension, where Green's axial strain

$$\varepsilon = \frac{1}{2}(\partial_s \boldsymbol{x} \cdot \partial_s \boldsymbol{x} - 1) \tag{10}$$

is used. Choosing a high value of the parameter b, we effectively penalize the axial extensibility, which, of course, requires a sufficiently fine spatial discretization so the approximation is compatible with this constraint. The expressions for κ and ε contain derivatives with respect to the material coordinate, which we rewrite in terms of the normalized coordinate:

$$\partial_s \boldsymbol{x} = \partial_\sigma \boldsymbol{x}\,\partial_s \sigma = \frac{1}{\eta}\partial_\sigma \boldsymbol{x}, \quad \partial_s^2 \boldsymbol{x} = \frac{1}{\eta^2}\partial_\sigma^2 \boldsymbol{x}. \tag{11}$$

The total kinetic energy of the rod

$$T = \int_0^1 \frac{1}{2}\rho \dot{\boldsymbol{x}} \cdot \dot{\boldsymbol{x}}\,\eta\,\mathrm{d}\sigma + \frac{1}{2}\rho(\ell - \eta)\dot{\eta}^2 \tag{12}$$

comprises the kinetic energy of the free segment (the first term with the integral) and the kinetic energy of the constrained part with a variable length inside the sleeve. It is convenient to decompose the material velocity of a particle in the free segment into a local time derivative and a convective term according to

$$\dot{\boldsymbol{x}} = \partial_t \boldsymbol{x}(\sigma(s,t),t)|_{s=\mathrm{const}} = \partial_t \boldsymbol{x}|_{\sigma=\mathrm{const}} + \dot{\sigma}\,\partial_\sigma \boldsymbol{x}, \tag{13}$$

while the time derivative of the normalized coordinate for a given material particle follows from the vanishing material time derivative of s in Eq. (2):

$$\dot{s} = 0 \quad \Rightarrow \quad -\dot{\eta} + \dot{\eta}\sigma + \eta\dot{\sigma} = 0 \quad \Rightarrow \quad \dot{\sigma} = \frac{(1-\sigma)\dot{\eta}}{\eta}. \tag{14}$$

It remains to express the total potential of the gravity force, which again comprises contributions from both the free and the constrained segments:

$$W = \int_0^1 \rho g(x\cos\alpha + y\sin\alpha)\eta\,\mathrm{d}\sigma - \frac{1}{2}\rho g\cos\alpha\,(\ell - \eta)^2; \tag{15}$$

the height of the center of gravity of the part within the sleeve equals $-\cos\alpha\,(\ell-\eta)/2$, and its mass is $\rho(\ell-\eta)$.

3. Equations of motion of a non-material finite element model

To numerically study the dynamics of a dancing rod, we discretize the deformation of the free segment by means of C^1-continuous finite elements in the spirit of Vetyukov (2012). The cubic Hermitian approximation provides the necessary degree of inter-element continuity and a rapid convergence rate, which is also beneficial in view of the inextensibility constraint.

We divide the non-material domain $0 \le \sigma \le 1$ into n finite elements. Nodes $\sigma_i = i/n$ are not bound to specific material particles. As opposed to the nodes, material particles travel across the finite element mesh. Components of the position vector $\boldsymbol{x}_i$ and its derivative $(\partial_\sigma \boldsymbol{x})_i$ constitute four scalar degrees of freedom of each node. The position of a point on an element between nodes i and $i+1$ reads

$$\boldsymbol{x}_{\text{element}}(\sigma) = S_1(\sigma)\boldsymbol{x}_i + S_2(\sigma)(\partial_\sigma \boldsymbol{x})_i + S_3(\sigma)\boldsymbol{x}_{i+1} + S_4(\sigma)(\partial_\sigma \boldsymbol{x})_{i+1} \tag{16}$$

with S_i, $i = 1, \dots, 4$, being the cubic shape functions guaranteeing C^1 inter-element continuity, i.e., that the deformed centerline remains smooth. The specific implementation relies on a referential element and a local coordinate, which allows us to use the same shape functions for all elements. According to the boundary conditions Eq. (5), we demand

$$x_0 = 0, \quad y_0 = 0, \quad (\partial_\sigma y)_0 = 0. \tag{17}$$

The remaining $4(n+1) - 3 + 1 = 4n + 2$ time-dependent generalized coordinates, which uniquely describe the configuration of the rod, are assembled into a column matrix

$$\mathrm{q} = \left[(\partial_\sigma x)_0, x_1, y_1, (\partial_\sigma x)_1, (\partial_\sigma y)_1, \dots, x_n, y_n, (\partial_\sigma x)_n, (\partial_\sigma y)_n, \eta\right]^T. \tag{18}$$

Note that the length of the free segment η belongs to the solution-dependent variables along with the nodal unknowns.

The approximation is able to accurately satisfy the inextensibility constraint with a relatively small number of elements: numerical experiments discussed below demonstrate that even for $n = 8$ the values of ε are very small. While we expect $\varepsilon \to 0$ for $n \to \infty$ and $b \to \infty$, too high values for the penalty stiffness b render the equations of motion ill-conditioned such that numerical solutions fail. Moreover, when penalizing ε, we introduce high frequency longitudinal vibration modes, which persist in the solution as the system is conservative. We gain numerical efficiency by letting these vibrations to quickly damp out using a dissipation function

$$R = \int_0^1 \frac{1}{2}\delta\dot{\varepsilon}^2\eta \, \mathrm{d}\sigma \tag{19}$$

with the damping parameter δ. For small ε, the energy dissipation is low and the effect of the dissipation function on the transverse bending oscillations is negligible. Choosing an appropriate small value of δ, we greatly reduce axial oscillations in the dynamic process and allow larger time steps in the adaptive time integration routine, thus accelerating the solver and reducing the memory consumption.[2]

The contributions of each finite element to integrals in Eqs. (8), (12), (15), (19) are computed using the 3-point Gaussian quadrature rule, which matches the approximation order. Assembling the contributions of all n finite elements, we obtain symbolic expressions for $U(\mathrm{q})$, $T(\mathrm{q}, \dot{\mathrm{q}})$, $W(\mathrm{q})$ and $R(\mathrm{q}, \dot{\mathrm{q}})$, which finally results into $4n + 2$ Lagrangian equations of motion

$$\frac{\mathrm{d}}{\mathrm{d}t}\left(\frac{\partial T}{\partial \dot{\mathrm{q}}}\right) - \frac{\partial T}{\partial \mathrm{q}} = -\frac{\partial U}{\partial \mathrm{q}} - \frac{\partial W}{\partial \mathrm{q}} - \frac{\partial R}{\partial \dot{\mathrm{q}}} \tag{20}$$

written for nodal unknowns and η.

4. Results of finite element simulations

The following numerical example demonstrates the application of the numerical model and is meant to show that the rod's dynamic behavior qualitatively depends on the slenderness ratio ℓ/h. For this purpose, we first consider a "thin" rod with a slenderness $\ell/h = 2000$; subsequently, the slenderness of the rod is reduced to $\ell/h = 500$. To contrast the first case, such rod is referred to as "thick" in what follows. This naming convention is justified by the observation that the dynamics of the thin rod is highly irregular and the transient process eventually ends up in a full ejection of the rod from the sleeve. The transient behavior of the thick rod is more regular due to the different time scales of the axial motion and transverse vibrations, which makes it also accessible to the analytical approach by means of the methods of nonlinear dynamics as demonstrated further in Section 6.

4.1. Thin and flexible rod

We begin simulations by considering a very flexible steel rod with a small thickness h: half a millimeter thickness over one meter length implies that the inertia dominates over the elastic resistance. The initially straight rod is inserted by 30% of its length into the sleeve inclined by 45°:

$$\begin{aligned} &\ell = 1, \quad h = 0.5 \cdot 10^{-3}, \quad E = 2.1 \cdot 10^{11}, \quad a = Eh^4/12, \quad b = Eh^2, \\ &\rho = 7800\,h^2, \quad \alpha = \pi/4, \quad \delta = 10, \quad \eta(0) = 0.7\ell, \end{aligned} \tag{21}$$

SI base units are used throughout the paper. The penalty stiffness b is chosen equal to the physical tension stiffness of the rod, as the considered slenderness ratio clearly guarantees negligible tensile strain in the absence of a particularly high axial loading. The chosen value of δ is small enough to not visibly affect the solution and is sufficiently large to increase the speed of time integration considerably.

[2] Wolfram Mathematica framework was applied for the symbolic derivation of equations of motion and their integration in time, see https://www.wolfram.com/mathematica/. The Wolfram Mathematica notebook with the simulation code is provided online as supplementary material to the present manuscript.

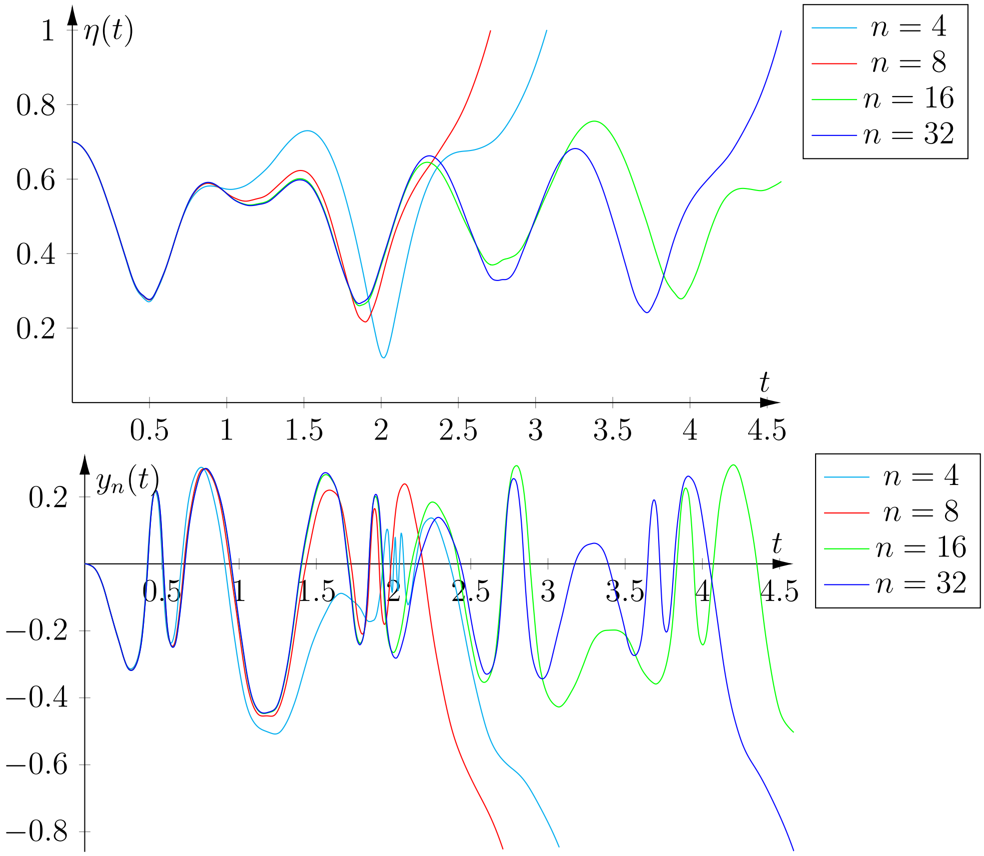

Fig. 2. Time histories of the length of the free part η and transverse tip deflection y_n for a thin rod, computed with different number of finite elements n; $\eta = 1$ corresponds to the full ejection.

Table 1
Maximum axial strain in dependence on the number of finite elements.

n	4	8	16	32
$\max \varepsilon$	$2.8 \cdot 10^{-4}$	$1.0 \cdot 10^{-4}$	$2.3 \cdot 10^{-5}$	$6 \cdot 10^{-6}$

The computed time histories of the configurational parameter $\eta(t)$ and the transverse tip deflection $y_n(t)$ are depicted in Fig. 2 for four different levels of finite element discretization. Despite highly irregular solutions, mesh convergence can be observed: solutions with 16 and 32 finite elements remain very close until $t \approx 2$, while the solution with just 4 finite elements "goes its own way" already at $t \approx 0.5$. In three out of four time histories, the dynamic process ends in full ejection $\eta = 1$ with subsequent free flying of the rod. Actually, the computation for $n = 16$ also ends in the full ejection, but at a later time $t = 6.27$. At the time instants of full ejection, deflections y_n are large and the free segment is strongly bent: as the energy is conserved, there is no elevation of the center of mass of the rod beyond the initial state — the rod slides out with the help of its high flexibility. A better impression of the dynamic process is conveyed by the animation, provided in the supplementary material. It would require an extensive series of numerical experiments to estimate the minimum initial length of the free segment $\eta(0)$, at which full ejection is still possible.

For the computed dynamic solutions, we evaluate how the maximum axial strain ε in the entire model depends on the discretization level. Data provided in Table 1 shows that the strain is indeed quickly getting negligible as the mesh is refined.

We conclude the discussion of the general validity of the developed simulation tool by mentioning that we also applied it to solve a slightly modified problem suggested by Han and Bauchau (2023): the sleeve is vertically aligned with the gravity and vibrations are excited by a transversely acting force at the tip of the rod. The obtained time histories of the tip deflections and velocity components were visually indistinguishable from the results in Han and Bauchau (2023). The latter result was also supported by a comparison to a full contact simulation using Abaqus, which indirectly validates present simulations.

4.2. Thick rod

Now we address a more realistic case of a less flexible rod with two millimeters thickness: $h = 2 \cdot 10^{-3}$, all other parameters remain the same as in Eq. (21). Simulation results, presented in Fig. 3, allow us to make the following observations.

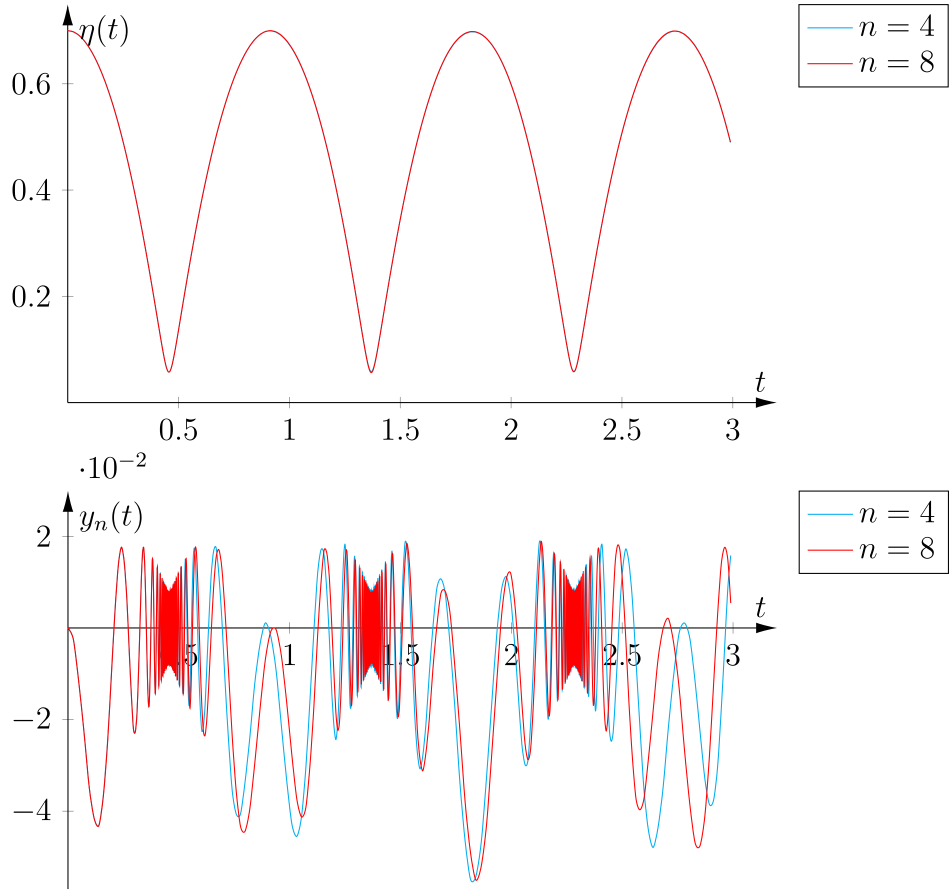

Fig. 3. Time histories of the length of the free part η and transverse tip deflection y_n for a thick rod, computed with different number of finite elements n.

- The process gets quasi-periodic: the rod moves up and down with periodicity clearly visible in $\eta(t)$.
- The amplitude of transverse vibrations y_n gets generally small compared to a characteristic scale of the axial motion.
- Two time scales determine the solution: $\eta(t)$ changes slowly in time, while the transverse vibrations are fast.
- The amplitude and the period of transverse oscillations become much smaller when the free part of the rod gets shorter, i.e. at small $\eta(t)$. The increase in the vibration frequency quite is dramatic: the period of oscillations changes by the factor of 100 or more.
- Solutions with 4 and 8 finite elements are indistinguishable in terms of the axial motion $\eta(t)$; the transverse oscillations demonstrate minor phase shift, which is not crucial for the overall dynamics.

During the motion, the rod periodically reaches the highest position η_{max}, which is very close to $\eta(0)$, and the lowest position η_{min}. This observation raises the natural question, whether it is possible to determine the dynamics of the axial motion $\eta(t)$ and the maximum injection depth $\max(\ell - \eta) = \ell - \eta_{\text{min}}$ semi-analytically, preferably in closed form. The positive answer will be given in Section 6.

4.3. Configurational force

We conclude the discussion of finite element solutions for a thick rod by presenting the time history of the x component of the acceleration of the center of mass of the rod in Fig. 4. The current coordinate of the center of mass $x_{\text{c.o.m.}}$ is computed analogously to W in Eq. (15) by setting $\rho g = 1/\ell$ and $\alpha = 0$, and the acceleration $\ddot{x}_{\text{c.o.m.}}$ follows after double numerical differentiation with respect to time. Besides the three narrow zones with small η and high frequency oscillations, the acceleration varies slightly around the value $-g\cos\alpha \approx -6.93$, which would correspond to the free falling of a rigid rod into the channel. The peaks reflect the rapid acceleration of the rod upwards because of the configurational force dominating over gravity when η is getting small. Second Newton's law allows computing the acceleration according to the formula

$$\begin{aligned} &\rho\ell\ddot{x}_{\text{c.o.m.}} = -\rho g\ell\cos\alpha + N, \\ &N = \frac{1}{2}a\kappa^2\Big|_{\sigma=0^+} \end{aligned} \tag{22}$$

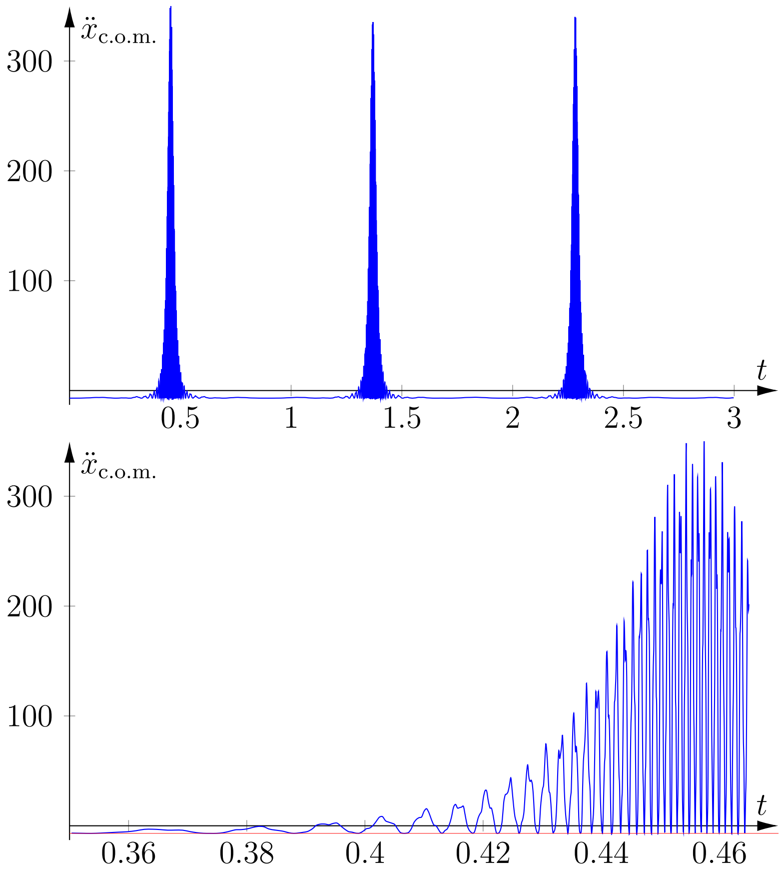

Fig. 4. Time history of the axial component of the acceleration of the center of mass of the rod for the model with $n = 4$ finite elements, plotted for the entire time domain and in the first time window of rapid acceleration. The reference acceleration value $-g\cos\alpha$ is depicted red..

with the configurational force N being equal to the strain energy density at the tip of the sleeve (Bigoni et al., 2022; Han and Bauchau, 2023); all other contact forces act in transverse direction. The plot of Eq. $(22)_1$ over time is visually indistinguishable from Fig. 4, which substantiates the consistency of the model.

5. Simplified two degree of freedom model

5.1. Basic assumptions and approximations

In this section, we develop and analyze a semi-analytical model based on two assumptions, the validity of which is supported by finite element analysis of the dynamics of the thicker rod.

- The overall bending deformation remains small, thus the strain energy of the free segment may be computed according to the geometrically linear beam theory.
- The first vibration mode dominates the solution.

This justifies the Ritz approximation for the deformed centerline of the free segment in terms of just two generalized coordinates:

$$\boldsymbol{x}(\sigma, t) = \eta(t)\sigma \boldsymbol{e}_x + \gamma(t) w(\sigma) \boldsymbol{e}_y. \tag{23}$$

Here, the length of the free segment $\eta(t)$ determines the axial motion, while the second generalized coordinate $\gamma(t)$ is the magnitude of the bending deformation. The shape function $w(\sigma)$ needs to be close to the first vibration mode. One possibility is to use the deformed shape of a cantilever under distributed load:

$$\partial_\sigma^4 w = \text{const}, \quad w(0) = \partial_\sigma w(0) = 0, \quad \partial_\sigma^2 w(1) = \partial_\sigma^3 w(1) = 0 \quad \Rightarrow \quad w = w_{\text{static}} = \frac{1}{3}(\sigma^4 - 4\sigma^3 + 6\sigma^2). \tag{24}$$

This static shape function is normalized by its value at the end: $w(1) = 1$, and is close to the exact vibration mode $w_{\text{dynamic}}(\sigma)$ following from the eigenvalue problem

$$\partial_\sigma^4 w = \lambda^4 w, \quad w(0) = \partial_\sigma w(0) = 0, \quad \partial_\sigma^2 w(1) = \partial_\sigma^3 w(1) = 0 \tag{25}$$

with the first eigenvalue $\lambda \approx 1.8751$; once again $w_{\mathrm{dynamic}}(1) = 1$. Both shape functions are used for comparison in the simulations, while the derivations below are presented only for the static one $w = w_{\mathrm{static}}$ for the sake of simplicity.

5.2. Energy expressions and equations of motion

The energy expressions, discussed in Section 2.3, may now be computed analytically. The axial strain vanishes because of the geometric linearity, and the bending strain simplifies to

$$\kappa = \gamma\, \partial_\sigma^2 w/\eta^2. \tag{26}$$

The strain energy becomes

$$U = \frac{1}{2} a\eta \int_0^1 \kappa^2 \,\mathrm{d}\sigma = \frac{a\gamma^2}{2\eta^3} \int_0^1 \frac{1}{9}(12\sigma^2 - 24\sigma + 12)^2 \,\mathrm{d}\sigma = \frac{8a\gamma^2}{5\eta^3}. \tag{27}$$

The material velocity of a particle Eq. (13) follows as

$$\dot{\boldsymbol{x}} = \dot\eta \boldsymbol{e}_x + \left(\dot\gamma w + \frac{1-\sigma}{\eta}\gamma\dot\eta\, \partial_\sigma w\right)\boldsymbol{e}_y, \tag{28}$$

and, after integration and substitution $w = w_{\mathrm{static}}$, the kinetic energy Eq. (12) is

$$T = \frac{\rho}{810}\left(104\dot\gamma(\eta\gamma)^{\cdot} + \frac{5(16\gamma^2 + 81\ell\eta)\dot\eta^2}{\eta}\right). \tag{29}$$

After dropping the constant term, the gravity potential Eq. (15) becomes

$$W = \rho g \ell \eta \cos\alpha + \frac{2}{5}\rho g \eta\gamma \sin\alpha. \tag{30}$$

We omit the dissipation function: there is no axial strain any more. The Lagrange equations of motion of the second kind Eq. (20) assume a highly nonlinear form

$$\begin{aligned} &52\rho\eta^4\gamma\ddot\gamma + 5\rho\eta^3(16\gamma^2 + 81\ell\eta)\ddot\eta + 2\rho\gamma\eta^3(81g\eta\sin\alpha + 80\dot\gamma\dot\eta) - 8\gamma^2(243a + 5\rho\eta^2\dot\eta^2) + 405\rho g\ell\eta^4\cos\alpha = 0,\\ &52\rho\eta^4\ddot\gamma + 26\rho\gamma\eta^3\ddot\eta + \rho\eta^3(81g\eta\sin\alpha + 52\dot\gamma\dot\eta) + 8\gamma(81a - 5\rho\eta^2\dot\eta^2) = 0. \end{aligned} \tag{31}$$

The structure of the equations remains the same with the dynamic shape function $w = w_{\mathrm{dynamic}}$. The numerical coefficients, though, are different.

5.3. Static equilibrium and configurational force

Prior to integrating the two degrees of freedom equations of motion over time, we investigate static equilibria. Equating the generalized force for γ to zero, we find

$$Q_\gamma = -\frac{\partial(U+W)}{\partial\gamma} = 0 \quad\Rightarrow\quad \gamma = -\frac{\rho g \eta^4 \sin\alpha}{8a}. \tag{32}$$

Now, we substitute this solution in the generalized force for η:

$$Q_\eta = -\frac{\partial(U+W)}{\partial\eta} = -\rho g\ell\cos\alpha + N, \quad N = \frac{\rho^2 g^2 \eta^4 \sin^2\alpha}{8a}. \tag{33}$$

The x component of the gravity and the configurational force N contribute to Q_η, see the first equality in Eq. (22) for comparison. The static equilibrium is possible when the equation $Q_\eta = 0$ has a solution for η smaller than ℓ. Interestingly, the determinant of the matrix of second derivatives of $U + W$ with respect to η and γ at static equilibrium equals $-8\rho^2 g^2 \sin^2\alpha$ and is always negative, which implies instability.

Substituting γ from Eq. (32) into the expression for the curvature, Eq. (26), we observe that the second equality in Eq. (22) is satisfied identically: N equals the strain energy density of the rod at the tip of the sleeve. While seeming rather natural, this property of the model is a consequence of the specific choice of the shape function $w_{\mathrm{static}}(\sigma)$, which exactly reproduces small static deformations under gravitational loading. Thus, choosing $w = w_{\mathrm{dynamic}}$ and repeating the computations, we arrive at N being greater than $a\kappa^2/2|_{\sigma=0^+}$ exactly by the factor 1.25. Despite the close proximity of the two shape functions, the solution for the equilibrium length of the free part then differs by a factor $1.25^{1/4} \approx 1.057$ from the exact solution.

5.4. Time integration of the equations of motion

Results of time integration of equations of motion Eq. (31) for the thick rod (parameter set as in Eq. (21) but with $h = 2\cdot 10^{-3}$, $\gamma(0) = 0$, $\dot\gamma(0) = 0$) are presented in Fig. 5 in comparison to the finite element solution with the coarse mesh $n = 4$. All solutions match well in terms of the axial motion $\eta(t)$. The transverse vibration $\gamma(t)$ corresponds to $y_n(t)$, although the phase difference is quickly getting accumulated because of the nonlinear interaction with higher vibrations modes, which are present in the solution to a small extent due to the initial conditions. The vibration amplitude and frequency as well as the axial motion are accurately captured by the simplified model. Models with the static and with the dynamic shape function remain at the same level of accuracy.

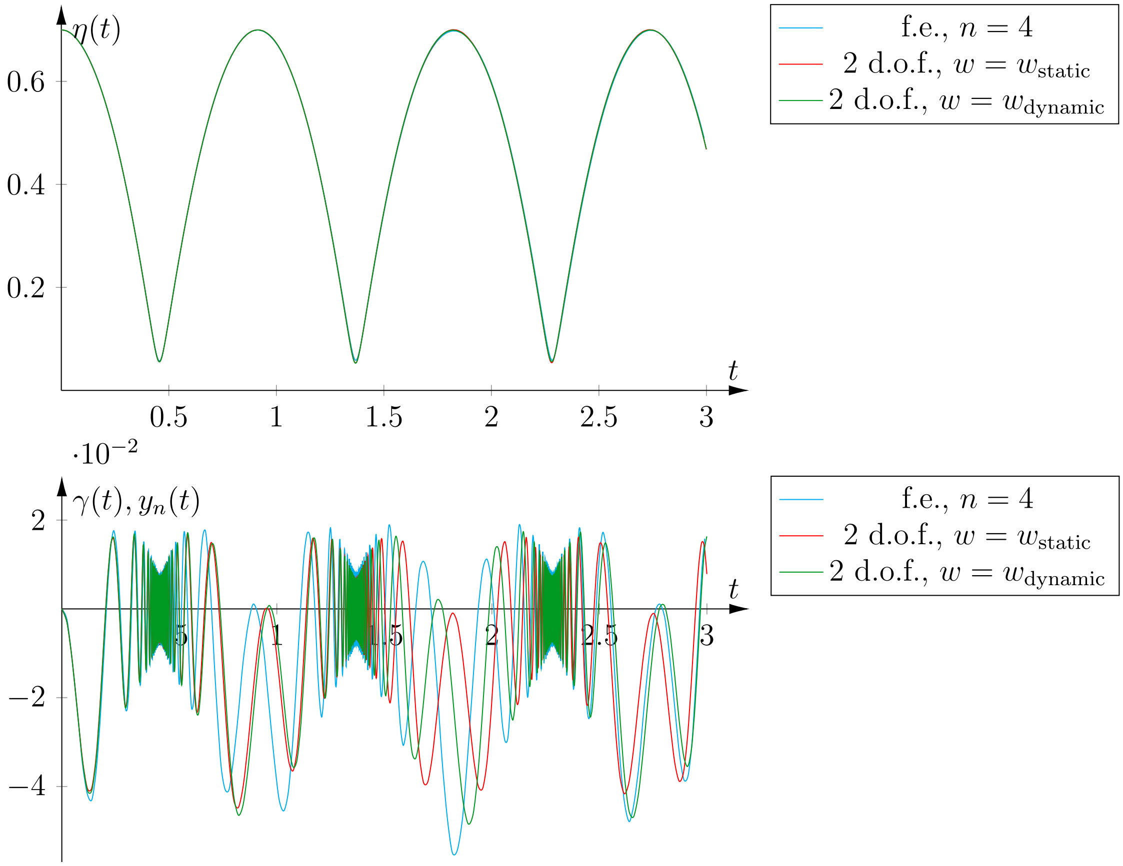

Fig. 5. Time histories of the length of the free part η and the transverse tip deflection γ for the thick rod, computed using the coarse finite element model and using the two degrees of freedom model with static and dynamic shape functions.

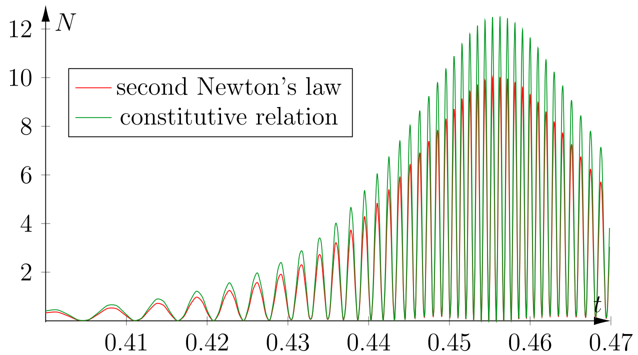

Fig. 6. Time histories of the configurational force for the two degrees of freedom simulation of the thick rod with $w = w_{\mathrm{static}}$, obtained using the Newton's second law Eq. (22)$_1$ and according to the constitutive relation Eq. (22)$_2$.

The time integration of the two degrees of freedom model is accomplished by Wolfram Mathematica ca. 1000 times quicker than that for the finite element model with 4 elements.

Similar to Section 4.3, we conclude the numerical investigation of the two degrees of freedom model by evaluating the configurational force in two ways according to the two expressions in Eq. (22). The respective time histories of N are depicted in Fig. 6 for a short time interval around the instant of maximum injection. The curve denoted as "second Newton's law" features the dynamic equation (22)$_1$ with $\ddot{\eta}$ substituted instead of $\ddot{x}_{\mathrm{c.o.m.}}$. The other curve, "constitutive relation", is obtained by computing N using the curvature at the tip of the sleeve $\kappa|_{\sigma=0^+} = 4\gamma/\eta^2$ according to Eq. (22)$_2$. The two time histories exactly scale by the factor 1.25. The reason is again the choice of the shape function: switching to w_{dynamic}, we would have obtained visually indistinguishable plots without any correction factor — and very close to the "second Newton's law" curve in Fig. 6. Clearly, one of the shape functions is more appropriate for the static analysis as in Section 5.3, while the other one fits the dynamic analysis. Interestingly, even the relative errors in both cases are identical. This inconsistency in the computation of the configurational force has, however, little impact on the simulated dynamics of the system itself.

6. Analytical investigation of the two degrees of freedom model

As mentioned previously, the two degrees of freedom of the simplified model behave differently from each other. On the one hand, $\eta(t)$ changes slowly, and the time scale of the axial motion is determined by the free falling of the rod into the inclined sleeve under gravity. On the other hand, $\gamma(t)$ is a quick vibration process, whose small amplitude and high frequency are determined by the actual length of the free segment. This is a good starting point for treating the nonlinear problem analytically with the following aims:

- To estimate how the instantaneous mean value, vibration amplitude, and frequency of the transverse vibrations $\gamma(t)$ depend on $\eta(t)$.
- To obtain a closed-form estimate for the minimum value of the length of the free segment $\eta_{\min} = \min \eta(t)$ and the maximum injection depth $\ell - \eta_{\min}$ during the quasi-periodic process.
- To derive a single differential equation for the axial motion $\eta(t)$, i.e., to eliminate γ.

We will elaborate on these results using the theory of adiabatic invariants, established in the field of nonlinear dynamics (Arnol'd, 1963); see also Zelenyi et al. (2013) for the application of such methods to physics of charged particles. Although normalized variables are often used in nonlinear dynamics, we found it beneficial to keep the description in terms of physical dimensional quantities to retain the connection to the numerical experiments, presented above. The analytical derivations are performed under the assumption of a high bending stiffness a and a small bending deformation γ. The accuracy of these approximate results will thus depend on the thickness of the rod, which has a direct influence on the ratio of the time scales and the amplitudes of the two kinds of motion. We proceed with the description of the system in terms of the Hamilton function, which is the starting point of the analysis.

6.1. Generalized momenta and series expansion of the Hamiltonian

The dynamics of the conservative system at hand is fully determined by the total potential $V(\eta,\gamma) = U + W$, Eqs. (27), (30), and by the kinetic energy T, Eq. (29), which has a quadratic form

$$T = \frac{1}{2}\dot{\mathrm{q}}^T \mathrm{M}(\mathrm{q})\dot{\mathrm{q}} \tag{34}$$

with $\mathrm{q} = [\eta,\gamma]^T$ and the mass matrix

$$\mathrm{M} = \rho \begin{bmatrix} \ell + \frac{16\gamma^2}{81\eta} & \frac{52}{405}\gamma \\ \frac{52}{405}\gamma & \frac{104}{405}\eta \end{bmatrix}. \tag{35}$$

The conjugate generalized momenta follow as

$$\mathrm{p} = \begin{bmatrix} p_\eta \\ p_\gamma \end{bmatrix} = \frac{\partial T}{\partial \dot{\mathrm{q}}} = \mathrm{M}\dot{\mathrm{q}}; \quad \dot{\mathrm{q}} = \mathrm{M}^{-1}\mathrm{p}. \tag{36}$$

The Hamilton function is the Legendre transformation of the Lagrange function $T - V$ with respect to $\dot{\mathrm{q}}$ and results into

$$H(\mathrm{q},\mathrm{p}) = \frac{1}{2}\mathrm{p}^T \mathrm{M}^{-1}(\mathrm{q})\mathrm{p} + V(\mathrm{q}). \tag{37}$$

The Hamiltonian H numerically equals the total energy $T + V$ and thus represents the first integral of the equations of motion.

At high bending stiffness, both γ and p_γ will be asymptotically smaller than η and p_η. Considering the asymptotic procedure as a tool for obtaining a closed-form approximate solution rather than as the principal aim of the investigation, we avoid non-dimensionalizing the equations and extracting a dimensionless parameter combination. Instead, we introduce a formal small parameter λ by replacing $\gamma \to \lambda\gamma$ and $p_\gamma \to \lambda p_\gamma$ in Eq. (37) and write the Hamiltonian in form of series expansion

$$H = H_0 + \lambda H_1 + \lambda^2 H_2 + O(\lambda^3) \tag{38}$$

with the contributions of different orders of magnitude:

$$\begin{aligned} H_0 &= \frac{p_\eta^2}{2\rho\ell} + \rho g \ell \eta \cos\alpha, \\ H_1 &= \frac{2}{5}\rho g \eta \gamma \sin\alpha, \\ H_2 &= \frac{1}{2}\Gamma^T \mathrm{A}\Gamma. \end{aligned} \tag{39}$$

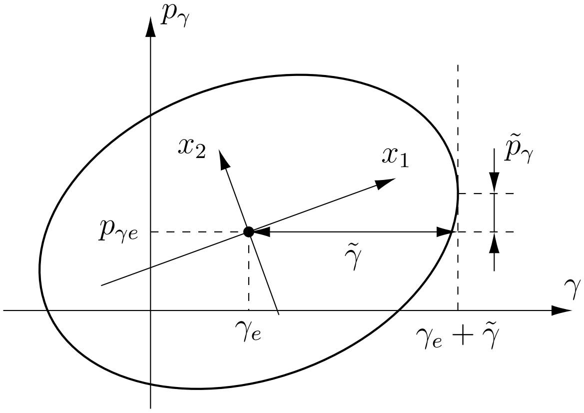

Fig. 7. Elliptic trajectory in the phase space of fast variables; the area of the ellipse remains approximately constant during the dynamic process.

The second-order term is a quadratic form of coordinates in the phase space of fast variables $\Gamma = [\gamma, p_\gamma]^T$ with a symmetric matrix

$$\mathrm{A} = \begin{bmatrix} \frac{16a}{5\eta^3} - \frac{2p_\eta^2}{15\rho\ell^2\eta} & -\frac{p_\eta}{2\rho\ell\eta} \\ -\frac{p_\eta}{2\rho\ell\eta} & \frac{405}{104\rho\eta} \end{bmatrix}. \tag{40}$$

In the following, we set $\lambda = 1$ implying that the respective terms in the series expansion Eq. (38) keep their orders of magnitude.

6.2. Adiabatic invariant approach

Keeping just the principal term H_0 in the series expansion Eq. (38), we clearly arrive at a rigid rod falling into a sleeve. The interesting effects are contained in H_1 and H_2. The prerequisites for the treatment by means of the theory of adiabatic invariants are satisfied, see Arnol'd (1963), chapter 2, section 3: we consider $\eta(t)$ and $p_\eta(t)$ as slowly varying parameters in order to determine the properties of the fast dynamic process of transverse vibrations. For fixed η, p_η, the phase trajectory $\Gamma(t)$ is an ellipse in the first approximation, i.e., a level curve $H = \text{const}$, see the illustration in Fig. 7. The basic idea of the approach is that, although the shape of the ellipse changes in the process of the slow motion $\eta(t)$, $p_\eta(t)$, its area remains approximately constant retaining its initial value. We denote this area by $2\pi I$, in which I is called adiabatic invariant.

The center of the elliptic trajectory $\Gamma_e = [\gamma_e, p_{\gamma e}]^T$ minimizes the Hamiltonian and follows from a linear system of equations:

$$\begin{aligned} &\Gamma_e = \arg\min H \quad \Rightarrow \quad \frac{\partial(H_1+H_2)}{\partial\Gamma}\Big|_{\Gamma=\Gamma_e} = \mathrm{A}\Gamma_e + \begin{bmatrix} 2/5\rho g\eta\sin\alpha \\ 0 \end{bmatrix} = 0 \quad \Rightarrow \\ &\Gamma_e = -\frac{g\sin\alpha}{\Delta}\begin{bmatrix} 81/52 \\ p_\eta/(5\ell) \end{bmatrix}, \quad \Delta = \det \mathrm{A} = \frac{2(81a\rho\ell^2 - 5p_\eta^2\eta^2)}{13\rho^2\ell^2\eta^4}, \end{aligned} \tag{41}$$

where we introduced the determinant Δ of the matrix A. The ellipse itself is determined by the constant value of a quadratic form

$$F = \frac{1}{2}(\Gamma - \Gamma_e)^T \mathrm{A}(\Gamma - \Gamma_e) = h_0 \tag{42}$$

with the energy level of transverse oscillations

$$h_0 = H|_{t=0} - H|_{\Gamma=\Gamma_e}, \quad H|_{t=0} = H_0|_{p_\eta=0,\eta=\eta_0} = \rho g\ell\eta_0\cos\alpha. \tag{43}$$

The specific expression for h_0 is complicated and is irrelevant for the final result. Now, we are in the position to determine the instantaneous amplitude of transverse vibrations $\tilde{\gamma}$ from the additional condition that, at maximum transverse deflection, the tangent to the elliptical trajectory Eq. (42) is parallel to the coordinate axis p_γ, see Fig. 7:

$$\tilde{\gamma} = \max\gamma - \gamma_e, \quad \frac{\partial\gamma}{\partial p_\gamma}\Big|_{\gamma=\gamma_e+\tilde{\gamma},\ p_\gamma=p_{\gamma e}+\tilde{p}_\gamma} = 0 \tag{44}$$

in which $\tilde{p}_\gamma$ is the vertical distance between the touching point of the vertical tangent and the center of the ellipse. Vertical tangent means that the vertical component of the gradient of the quadratic form at the left hand side of Eq. (42) vanishes:

$$\frac{\partial F}{\partial p_\gamma} = 0 \quad \Rightarrow \quad A_{12}\tilde{\gamma} + A_{22}\tilde{p}_\gamma = 0 \quad \Rightarrow \quad \tilde{p}_\gamma = -A_{12}/A_{22}. \tag{45}$$

Substituting this expression into Eq. (42), we find the vibration amplitude:

$$(A_{11} - 2A_{12}^2/A_{22} + A_{22}(-A_{12}/A_{22})^2)\tilde{\gamma}^2 = 2h_0 \quad \Rightarrow \quad \tilde{\gamma} = \sqrt{2A_{22}h_0/\Delta}. \tag{46}$$

Numerical experiments show that the obtained approximation indeed corresponds well to the exact process $\gamma(t)$: plotting $\gamma_e \pm \tilde{\gamma}$ in Fig. 9, we obtain upper and lower envelopes, accurately outlining the extremes. The obtained result, however, is of little practical use because of the complexity of the expression of h_0. Therefore, we make a further step and compute the area of the ellipse which, in the principal coordinates x_1, x_2, fulfills the equation

$$\sigma_1 x_1^2 + \sigma_2 x_2^2 = 2h_0; \tag{47}$$

here, $\sigma_{1,2}$ are the eigenvalues of the matrix A. Clearly, the semi-axes of the ellipse are equal to $\sqrt{2h_0/\sigma_1}$ and $\sqrt{2h_0/\sigma_2}$, and the known formula for the area of an ellipse results into

$$2\pi I = \pi\sqrt{2h_0/\sigma_1}\sqrt{2h_0/\sigma_2} = 2\pi h_0/\sqrt{\Delta} \tag{48}$$

because $\sigma_1\sigma_2 = \Delta$. Substituting $h_0 = I\sqrt{\Delta}$ in Eq. (46), we find the amplitude as

$$\tilde{\gamma} = \sqrt{2A_{22}I/\sqrt{\Delta}} \tag{49}$$

with I being the adiabatic invariant, whose value is approximately known from the initial conditions:

$$I \approx I_0 = I|_{t=0} = h_0/\sqrt{\Delta}\Big|_{\eta=\eta_0,\ p_\eta=0} = \frac{\sqrt{13\rho^5}g^2\eta_0^7\sin^2\alpha}{360\sqrt{2a^3}}. \tag{50}$$

We substitute this approximation in Eq. (49) and use a further simplification that is fully supported by the results of numerical experiments: in the numerator of the expression for the determinant Δ in Eq. $(41)_2$, we neglect the term $5p_\eta^2\eta^2$ in comparison to $81a\rho\ell^2$, because the bending stiffness is high and the order of smallness of the slow dynamic term remains the same. These two assumptions produce a simple approximation of the vibration amplitude in dependence on the length of the free segment:

$$\tilde{\gamma} \approx \hat{\gamma} = \frac{\rho g}{8a}\sqrt{\eta_0^7\eta}\sin\alpha. \tag{51}$$

Using the simplified expression for Δ in Eq. $(41)_2$, we find another approximation for the instantaneous mean deflection of the end of the rod, which corresponds to the static solution for a beam under distributed weight:

$$\gamma_e \approx \hat{\gamma}_e = -\frac{\rho g\eta^4\sin\alpha}{8a}. \tag{52}$$

Now that we know the envelopes for $\gamma(t)$, we seek to find an estimate for the time-varying vibration frequency. The simplest way is just to use the second equation of motion Eq. $(31)_2$ (as this equation corresponds to the generalized coordinate γ). With $\dot{\eta} = 0$ and $\ddot{\eta} = 0$ the differential equation simplifies to

$$52\rho\eta^4\ddot{\gamma} + 648a\gamma + 81\rho g\eta^4\sin\alpha = 0. \tag{53}$$

The static solution corresponds to the already obtained expression Eq. (52), and the coefficients at γ and $\ddot{\gamma}$ produce an estimate for the instantaneous frequency

$$\omega = \sqrt{\frac{2a}{13\rho}}\frac{9}{\eta^2}. \tag{54}$$

This explains the drastic growth of the vibration frequency when the free segment is getting shorter. As we will see in the following, the approximation

$$\gamma(t) \approx \hat{\gamma}_e + \hat{\gamma}\cos\tau, \quad \dot{\tau} = \omega, \quad \tau(0) = 0 \tag{55}$$

with the time integration of the phase $\tau(t)$ provides an accurate match with results obtained by numerical integration. In summary, we emphasize that, although estimates for $\hat{\gamma}_e$ and ω are accessible by simple methods, the adiabatic invariant approach is required to obtain the amplitude $\hat{\gamma}$.

6.3. Maximum injection depth and dynamics of slow axial motion

Now that we established a relation between the transverse vibrations and the axial motion, we are in the position to analytically investigate the properties of the latter. The quasi-periodicity of the slow axial motion is the known theoretical result (Arnol'd, 1963). The balance of energy provides the simplest option to conclude on the maximum injection depth. The total mechanical energy of the conservative system remains at the initial value, computed above in Eq. (43) as $H|_{t=0}$. In accordance with Eqs. (51), (52), in the state of maximum injection, we have

$$\eta = \eta_{\min}, \quad \dot{\eta} = 0, \quad \tilde{\gamma} = \frac{\rho g}{8a}\sqrt{\eta_0^7\eta_{\min}}\sin\alpha, \quad \gamma_e = 0. \tag{56}$$

Indeed, we observe $\eta_{\min} \ll \eta_0$ in numerical simulations, such that the fourth power of $\eta_{\min}$ is very small in Eq. (52): the action of gravity on the transverse bending becomes negligible. We approximate the total mechanical energy at the instant of maximum injection as the gravity potential related to the axial motion plus the amplitude of the strain energy Eq. (27) due to the transverse vibration:

$$E_{\text{max.injection}} = W|_{\eta=\eta_{\min},\gamma=0} + U|_{\eta=\eta_{\min},\gamma=\bar{\gamma}} = \rho g \ell \eta_{\min} \cos\alpha + \frac{\rho^2 g^2 \eta_0^7 \sin^2\alpha}{40 a \eta_{\min}^2}. \tag{57}$$

The condition $E_{\text{max.injection}} = H|_{t=0}$ provides a cubic equation

$$40 a \ell (\eta_0 - \eta_{\min}) \eta_{\min}^2 \cos\alpha - \rho g \eta_0^7 \sin^2\alpha = 0. \tag{58}$$

Among the three roots of the equation, one approximately equals η_0 (because the initial state also satisfies conditions Eq. (56) only approximately), another is negative, and the third root is the actual minimum length of the free part. If we neglect $\eta_{\min}$ in comparison to η_0 in the parentheses of the first term of the equation, a simple analytical expression follows:

$$\eta_{\min} = \frac{\sqrt{\rho g \eta_0^3} \sin\alpha}{2\sqrt{10 a \ell \cos\alpha}}. \tag{59}$$

We now aim at deriving a single differential equation for the slow axial motion $\eta(t)$, and we achieve this goal using a straightforward averaging procedure. Using computer algebra, we perform the following mathematical transformations:

1. We substitute the approximation for $\gamma(t)$ Eq. (55) into the first equation of motion in Eq. $(31)_1$, taking into account the known estimate for the time derivative of the phase $\tau(t)$.
2. All terms containing $\sin\tau$, $\cos\tau$ or their products/powers are averaged over the period $0 \le \tau < 2\pi$, thus keeping only η and its time derivatives in the equation.
3. We simplify the equation, dividing it by the large bending stiffness a and neglecting the terms of order a^{-1} and smaller.

The obtained equation for the slow dynamics reads

$$40 a \ell (\ddot{\eta} + g\cos\alpha) - \rho g^2 (2\eta_0^7 \eta^{-3} + 5\eta^4) \sin^2\alpha = 0. \tag{60}$$

Alternatively, we may use the apparatus of analytical mechanics to reach this goal. Exactly the same equation of motion results after the following steps:

1. The "slow" Hamiltonian is computed as $H_{\text{slow}} = H|_{\Gamma=\Gamma_e} + I_0\sqrt{\Delta}$, in which we used an approximate expression for h_0, see Eqs. (43) and (50).
2. We keep just the terms of orders a^1 and a^0 in H_{slow} to simplify the expression.
3. System of equations $\dot{p}_\eta = -\partial H_{\text{slow}}/\partial\eta$, $\dot{\eta} = \partial H_{\text{slow}}/\partial p_\eta$ is transformed to a single second-order differential equation by excluding p_η.

Besides the possibility of efficient time integration, Eq. (60) provides an alternative way to get the value of $\eta_{\min}$. Writing it as $\ddot{\eta} = f(\eta)/2$, multiplying by $2\dot{\eta}$ and integrating over time we find

$$\dot{\eta}^2 = \int_{\eta_0}^{\eta} f(\tilde{\eta})\,\mathrm{d}\tilde{\eta} \quad \Rightarrow \quad \int_{\eta_0}^{\eta_{\min}} f(\eta)\,\mathrm{d}\eta \tag{61}$$

because the velocity vanishes in the state of maximum injection. Evaluating the integral, we arrive at an equation for $\eta_{\min}$, which slightly differs from Eq. (58): in the second term instead of η_0^7 we now have $\eta_0^7 - \eta_{\min}^7$, which has practically no influence on the root of the equation because of the smallness of $\eta_{\min}$.

Another practical result following from Eq. (60) is the acceleration and the average configurational force, reached in the state of maximum injection. Substituting $\eta = \eta_{\min}$ in the form of Eq. (59), solving for $\ddot{\eta}$ and neglecting the small term of order a^{-3}, we find an expression for $\ddot{\eta}_{\max}$. Substituting this expression in Newton's second law, we compute the maximum of the average configurational force:

$$\bar{N}_{\max} = \rho \ell \ddot{\eta}_{\max} + \rho g \ell \cos\alpha = \frac{4\sqrt{10 \rho g \ell^3 a \cos^3\alpha}}{\eta_0^2 \sin\alpha}. \tag{62}$$

6.4. Numerical validation of the theoretical results

The theoretical findings of the previous subsection are compared against the results of the time integration as in Section 5.4. We begin with validating the cornerstone of the analytical study, namely the invariance of the area of the ellipse in the phase space of fast variables $2\pi I$ according to Eq. (48) on the solutions of the equations of motion. In Fig. 8, we plot the ratio of the changing adiabatic invariant I to its initial value Eq. (50), based on the numerically obtained time histories $\eta(t)$, $\gamma(t)$. Although the value of I is not exactly conserved, it keeps oscillating in the vicinity of the initial value. Higher oscillations occur when the injection is small, as the time scale of the transverse vibration process is getting comparable to the time period of the axial motion. Moreover, at growing rod thickness h the oscillations are clearly getting smaller, which confirms the asymptotic accuracy of the adiabatic invariance for increasing bending stiffness a.

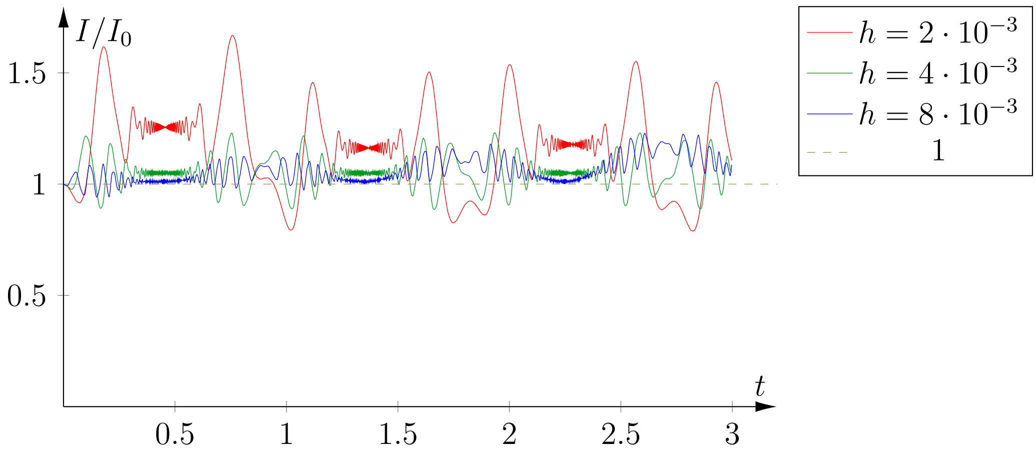

Fig. 8. Relative change of the area of the elliptic trajectory in the phase space of fast variables Eq. (48) in comparison to the initial value, based on Eq. (50).

Table 2
Minimum length of the free part $\eta_{\min}$ after the initial injection in dependence on the rod thickness h: analytical approximation in comparison to the numerical results with different models.

Thickness	Analyt. Eq. (59)	Slow dyn. Eq. (60)	2 d.o.f. Eq. (31)	F.e. $n = 4$
$1 \cdot 10^{-3}$	0.095312	0.103227	0.132680	0.135763
$2 \cdot 10^{-3}$	0.047656	0.049434	0.055653	0.057314
$4 \cdot 10^{-3}$	0.023828	0.024252	0.024858	0.025512
$8 \cdot 10^{-3}$	0.011914	0.012018	0.012087	0.012372

Motivated by this result, we proceed to comparing the approximation of the transverse vibration process $\gamma(t)$ to the results of the time integration in Fig. 9. We used the time history of $\eta(t)$ from the full system of equations of motion for the sake of evaluation of Eqs. (52)–(55). The quality of the approximation is good for the thick rod and is getting even better at growing h.

Finally, we proceed to the validation of the analytical results concerning the slow axial motion $\eta(t)$. In Table 2, we present the values of the minimum length of the free part $\eta_{\min}$ in dependence on the rod thickness h.

To validate simple analytical formula Eq. (59), we use results of time integration of the simplified equation of the slow dynamics Eq. (60), of the equations of motion of the two degree of freedom system Eq. (31) as well as of the finite element model with 4 elements. Post-processing the numerical results, we seek the minimum of $\eta(t)$ after the initial phase of injection at $t \approx 0.4$. The presented data confirms the increasing accuracy of the analytical approximation at growing bending stiffness. We also see that the predictions, made from the single differential equation (60) match well the results of time integration of the full two degrees of freedom model, which is additionally confirmed by the time histories of $\eta(t)$ in Fig. 10. We conclude the investigation by evaluating the highest mean configurational force Eq. (62). Substituting the parameter values for the thick rod with $h = 2 \cdot 10^{-3}$, we obtain $\bar{N}_{\max} = 6.35$. This value corresponds well to the running average of the force, computed according to the constitutive relation Eq. $(22)_2$ in Fig. 6.

7. Conclusions

The present investigation of the dynamics of a flexible rod sliding in an ideal frictionless sleeve in the field of gravity is based on methods ranging from a non-material finite element scheme to the analytical treatment in the framework of Hamiltonian mechanics and the adiabatic invariant approach. The finite element model is suitable for large oscillations, which is essential for very flexible rods. In this case, the motion becomes highly irregular, injections alternates with ejections, and even complete ejection is possible. For less flexible rods, the semi-analytical two degrees of freedom model produces accurate results for small vibrations. The subsequent analytical investigation provides closed-form estimates for characteristic values of the dynamic process such as the maximum injection depth of the rod before the configurational force turns injection into ejection. Further studies of the problem at hand could focus on the influence of friction and the flexibility of the sleeve, which is necessary for practically relevant formulations such as concentric tube robots used in medicine.

CRediT authorship contribution statement

Yury Vetyukov: Writing – review & editing, Writing – original draft, Visualization, Software, Project administration, Investigation, Formal analysis, Conceptualization. **Alexander Humer:** Writing – review & editing, Investigation, Conceptualization. **Alois Steindl:** Writing – review & editing, Methodology, Formal analysis.

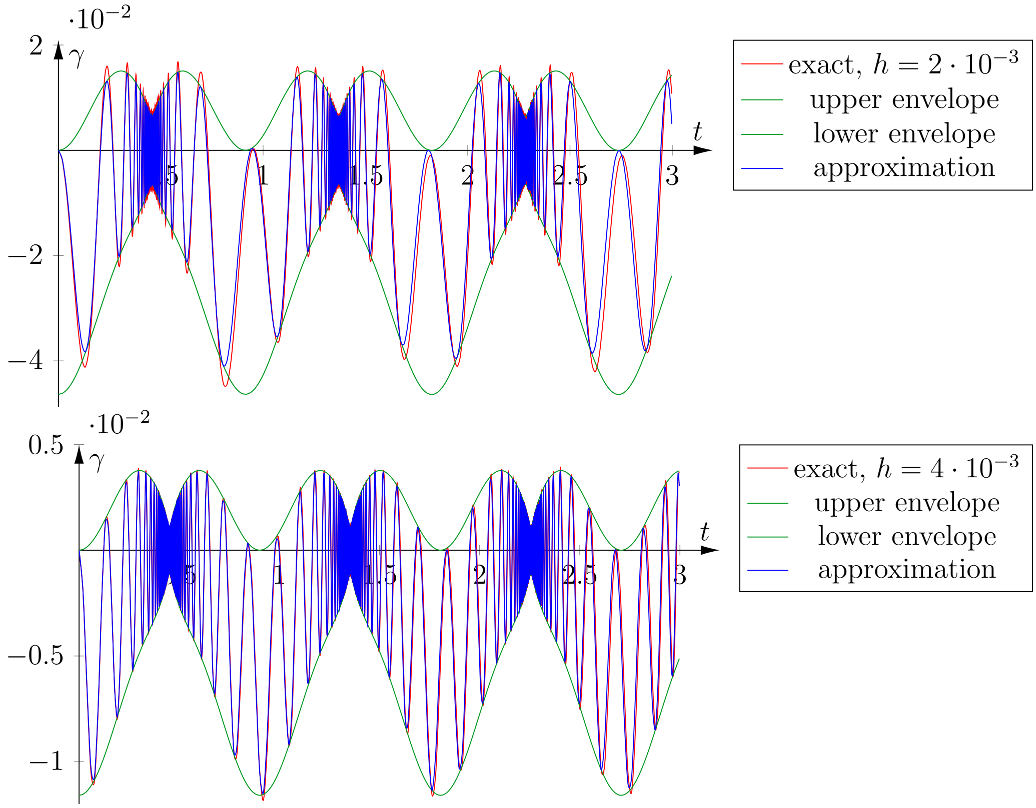

Fig. 9. Transverse vibrations $\gamma(t)$ resulting from the integration of the equation of motion for two values of the rod thickness h in comparison to the approximation Eq. (55) as well as upper and lower envelopes $\hat{\gamma}_e \pm \hat{\gamma}$.

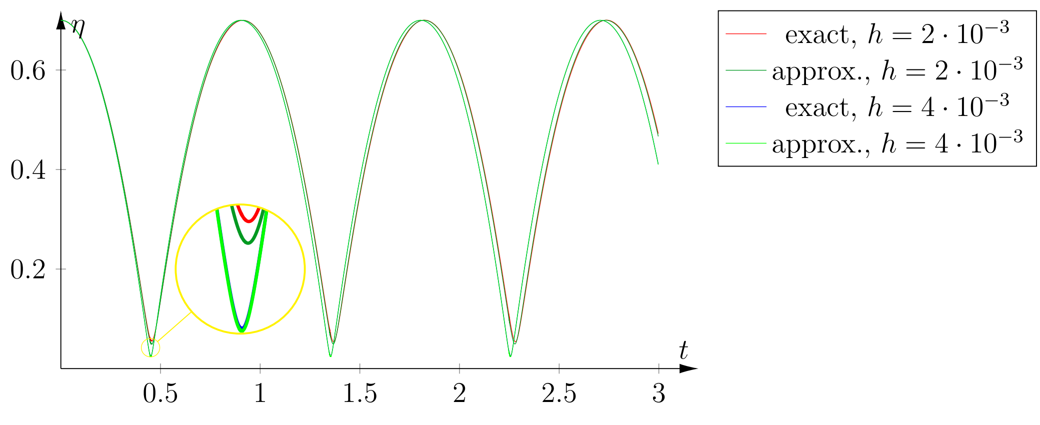

Fig. 10. Axial motion $\eta(t)$, computed according to the exact equations for the 2 d.o.f. model and the approximate equation for the slow dynamics Eq. (60) for two values of the thickness of the rod.

Declaration of competing interest

The authors declare the following financial interests/personal relationships which may be considered as potential competing interests: Yury Vetyukov reports article publishing charges was provided by TU Wien University. If there are other authors, they declare that they have no known competing financial interests or personal relationships that could have appeared to influence the work reported in this paper.

Data availability

Simulation code submitted as supplementary material.

Acknowledgment

The authors acknowledge TU Wien Bibliothek for financial support through its Open Access Funding Programme.

Appendix A. Supplementary data

Supplementary material related to this article can be found online at https://doi.org/10.1016/j.jmps.2024.105854.

References

Armanini, C., Dal Corso, F., Misseroni, D., Bigoni, D., 2019. Configurational forces and nonlinear structural dynamics. J. Mech. Phys. Solids 130, 82–100. http://dx.doi.org/10.1016/j.jmps.2019.05.009.

Arnol'd, V.I., 1963. Small denominators and problems of stability of motion in classical and celestial mechanics. Russian Math. Surveys 18 (6), 85. http://dx.doi.org/10.1070/RM1963v018n06ABEH001143.

Bigoni, D., Bosi, F., Dal Corso, F., Misseroni, D., 2022. Configurational forces on elastic structures. In: 50+ Years of AIMETA: A Journey Through Theoretical and Applied Mechanics in Italy. Springer, pp. 229–241. http://dx.doi.org/10.1007/978-3-030-94195-6_14.

Bigoni, D., Dal Corso, F., Bosi, F., Misseroni, D., 2015. Eshelby-like forces acting on elastic structures: theoretical and experimental proof. Mech. Mater. 80, 368–374. http://dx.doi.org/10.1016/j.mechmat.2013.10.009.

Bosi, F., Misseroni, D., Dal Corso, F., Bigoni, D., 2014. An elastica arm scale. Proc. R. Soc. A 470 (2169), 20140232. http://dx.doi.org/10.1098/rspa.2014.0232.

Boyer, F., Lebastard, V., Candelier, F., Renda, F., 2022. Extended Hamilton's principle applied to geometrically exact Kirchhoff sliding rods. J. Sound Vib. 516, 116511. http://dx.doi.org/10.1016/j.jsv.2021.116511.

Dal Corso, F., Amato, M., Bigoni, D., 2024. Elastic solids under frictionless rigid contact and configurational force. J. Mech. Phys. Solids 105673. http://dx.doi.org/10.1016/j.jmps.2024.105673.

Escalona, J.L., Orzechowski, G., Mikkola, A.M., 2018. Flexible multibody modeling of reeving systems including transverse vibrations. Multibody Syst. Dyn. 44, 107–133. http://dx.doi.org/10.1007/s11044-018-9619-6.

Han, S., 2022. Configurational forces and geometrically exact formulation of sliding beams in non-material domains. Comput. Methods Appl. Mech. Engrg. 395, 115063. http://dx.doi.org/10.1016/j.cma.2022.115063.

Han, S., Bauchau, O.A., 2023. Configurational forces in variable-length beams for flexible multibody dynamics. Multibody Syst. Dyn. 58 (3), 275–298. http://dx.doi.org/10.1007/s11044-022-09866-5.

Humer, A., 2013. Dynamic modeling of beams with non-material, deformation-dependent boundary conditions. J. Sound Vib. 332 (3), 622–641. http://dx.doi.org/10.1016/j.jsv.2012.08.026.

Humer, A., Steinbrecher, I., Vu-Quoc, L., 2020. General sliding-beam formulation: A non-material description for analysis of sliding structures and axially moving beams. J. Sound Vib. 480, 115341. http://dx.doi.org/10.1016/j.jsv.2020.115341.

Irschik, H., Holl, H., 2002. The equations of Lagrange written for a non-material volume. Acta Mech. 153, 231–248. http://dx.doi.org/10.1007/BF01177454.

Kaczmarczyk, S., Ostachowicz, W., 2003. Transient vibration phenomena in deep mine hoisting cables. Part 1: Mathematical model. J. Sound Vib. 262 (2), 219–244. http://dx.doi.org/10.1016/S0022-460X(02)01137-9.

Kienzler, R., Herrmann, G., 2000. Mechanics in Material Space: with Applications to Defect and Fracture Mechanics. Springer Science & Business Media, http://dx.doi.org/10.1007/978-3-642-57010-0.

Koutsogiannakis, P., Misseroni, D., Bigoni, D., Dal Corso, F., 2023. Stabilization against gravity and self-tuning of an elastic variable-length rod through an oscillating sliding sleeve. J. Mech. Phys. Solids 181, 105452. http://dx.doi.org/10.1016/j.jmps.2023.105452.

Mansfield, L., Simmonds, J., 1987. The reverse spaghetti problem: drooping motion of an elastica issuing from a horizontal guide. J. Appl. Mech. 54 (1), 147–150. http://dx.doi.org/10.1115/1.3172949.

Oborin, E., Vetyukov, Y., Steinbrecher, I., 2018. Eulerian description of non-stationary motion of an idealized belt-pulley system with dry friction. Int. J. Solids Struct. 147, 40–51. http://dx.doi.org/10.1016/j.ijsolstr.2018.04.007.

O'Reilly, O.M., 2017. Modeling Nonlinear Problems in the Mechanics of Strings and Rods. Springer, http://dx.doi.org/10.1007/978-3-319-50598-5.

Pechstein, A., Gerstmayr, J., 2013. A Lagrange–Eulerian formulation of an axially moving beam based on the absolute nodal coordinate formulation. Multibody Syst. Dyn. 30, 343–358. http://dx.doi.org/10.1007/s11044-013-9350-2.

Scheidl, J., Vetyukov, Y., 2023. Review and perspectives in applied mechanics of axially moving flexible structures. Acta Mech. 234 (4), 1331–1364. http://dx.doi.org/10.1007/s00707-023-03514-5.

Singh, H., Hanna, J., 2017. Pick-up and impact of flexible bodies. J. Mech. Phys. Solids 106, 46–59. http://dx.doi.org/10.1016/j.jmps.2017.04.019.

Steinbrecher, I., Humer, A., Vu-Quoc, L., 2017. On the numerical modeling of sliding beams: A comparison of different approaches. J. Sound Vib. 408, 270–290. http://dx.doi.org/10.1016/j.jsv.2017.07.010.

Steinmann, P., 2008. On boundary potential energies in deformational and configurational mechanics. J. Mech. Phys. Solids 56 (3), 772–800. http://dx.doi.org/10.1016/j.jmps.2007.07.001.

Vetyukov, Y., 2012. Hybrid asymptotic-direct approach to the problem of finite vibrations of a curved layered strip. Acta Mech. 223 (2), 371–385. http://dx.doi.org/10.1007/s00707-011-0562-3.

Vetyukov, Y., 2018. Non-material finite element modelling of large vibrations of axially moving strings and beams. J. Sound Vib. 414, 299–317. http://dx.doi.org/10.1016/j.jsv.2017.11.010.

Vetyukov, Y., 2021. Endless elastic beam travelling on a moving rough surface with zones of stick and sliding. Nonlinear Dynam. 104 (4), 3309–3321. http://dx.doi.org/10.1007/s11071-021-06523-y.

Vu-Quoc, L., Li, S., 1995. Dynamics of sliding geometrically-exact beams: large angle maneuver and parametric resonance. Comput. Methods Appl. Mech. Engrg. 120 (1–2), 65–118. http://dx.doi.org/10.1016/0045-7825(94)00051-N.

Zelenyi, L.M., Neishtadt, A.I., Artemyev, A.V., Vainchtein, D.L., Malova, H.V., 2013. Quasiadiabatic dynamics of charged particles in a space plasma. Phys.-Usp. 56 (4), 347. http://dx.doi.org/10.3367/UFNe.0183.201304b.0365.